metals

MDPI

Article

The Formation Mechanism of Oxide Inclusions in a High-Aluminum Ni-Based Superalloy during the Vacuum Induction Remelting Process

Lihui Zhang [1,†], Erkang Liu [2,†], Weijie Xing [1], Zhaojiang Xue [2], Wenjie Fan [2], Yunsong Zhao [1,*], Yushi Luo [1], Changchun Ge [2] and Min Xia [2,*]

[1] Science and Technology on Advanced High Temperature Structural Materials Laboratory, Beijing Institute of Aeronautical Materials, Beijing 100095, China; lihui.zhang@biam.ac.cn (L.Z.); xingwj621@163.com (W.X.); luoyushi1978@sohu.com (Y.L.)

[2] Institute of Powder Metallurgy and Advanced Ceramics, University of Science and Technology Beijing, Beijing 100083, China; liu18203224277@163.com (E.L.); zhaojiang_xue@163.com (Z.X.); wejiefan2022@163.com (W.F.); ccge@mater.ustb.edu.cn (C.G.)

* Correspondence: yunsong.zhao@biam.ac.cn (Y.Z.); xmdsg@ustb.edu.cn (M.X.)

† These authors contributed equally to this work.

Abstract: Oxide inclusions in Ni-based superalloys play a crucial role in determining their mechanical properties, oxidation resistance, and corrosion resistance at high temperatures. In this paper, the source and formation mechanism of different types of oxide inclusions in a high-aluminum Ni-based superalloy were systematically studied. An automatic field emission scanning electron microscope equipped with an energy dispersive spectrometer and a self-designed superalloy inclusion analysis standard was utilized to quantitatively reveal the oxide inclusion characteristics of the high-aluminum Ni-based superalloy prepared via vacuum induction melting (VIM) and vacuum induction remelting (VIR) processes. The experimental results indicate that the typical oxide inclusions in the Ni-based superalloy before the VIR process are irregular $MgO{\cdot}Al_2O_3$ inclusions with sizes of less than 2 μm. After the VIR process, the typical oxide inclusions in the Ni-based superalloy are also $MgO{\cdot}Al_2O_3$ inclusions. However, these oxide inclusions can be classified into three categories: (i) endogenous irregular $MgO{\cdot}Al_2O_3$ inclusions, less than 4.3 μm in size, inherited from the master alloy; (ii) several hundred-micron film-like $MgO{\cdot}Al_2O_3$ inclusions generated as interface reaction products between the MgO crucible and melts; and (iii) millimeter-scale $MgO{\cdot}Al_2O_3$ inclusions and several tens of microns of MgO inclusions from the exfoliation of the MgO crucible matrix.

Keywords: oxide inclusion; formation mechanism; interface reaction; vacuum induction remelting; Ni-based superalloy

Citation: Zhang, L.; Liu, E.; Xing, W.; Xue, Z.; Fan, W.; Zhao, Y.; Luo, Y.; Ge, C.; Xia, M. The Formation Mechanism of Oxide Inclusions in a High-Aluminum Ni-Based Superalloy during the Vacuum Induction Remelting Process. *Metals* **2024**, *14*, 654. https://doi.org/10.3390/met14060654

Academic Editor: Martin Heilmaier

Received: 26 April 2024
Revised: 23 May 2024
Accepted: 29 May 2024
Published: 30 May 2024

1. Introduction

Ni-based superalloys have been extensively applied in the aerospace industry due to their excellent mechanical properties, oxidation resistance, and corrosion resistance at high temperatures [1–3]. Investment casting is widely used in the manufacturing of high-temperature alloy components. During the alloy melting process, the contact between the high-temperature alloy liquid and refractory materials inevitably produces inclusions. Inevitably present in superalloy components, non-metallic inclusions serve as a key indicator for measuring the performance of Ni-based superalloys [4]. These seemingly small non-metallic inclusions are likely to be the nucleation locations of fatigue cracks, leading to the failure of superalloy components and even threatening people's lives [5–7]. Therefore, the characteristics of non-metallic inclusions in superalloys, such as their morphology, number, and distribution, should be seriously considered.

The common non-metallic inclusions in Ni-based superalloys are oxides, sulfides, carbides, etc., whereas oxide inclusions have received extensive attention [8–10]. In Ni-based

superalloys, oxide inclusions may seriously affect the safety performance of superalloy components due to the large differences in the elastic modulus, deformation ability, and high temperature–oxidation resistance between the oxide inclusion and the matrix [11,12]. In October 2016, a high-pressure turbine disk made of an Inconel 718 alloy on the US B767-300 aircraft broke during takeoff at Chicago O'Hare International Airport. The investigation indicated that a large-sized film-like $MgO{\cdot}Al_2O_3$–TiN inclusion cluster in the turbine disk became the initiation location of a fatigue crack, which ultimately caused the accident [13]. Nevertheless, not every oxide inclusion in nickel-based superalloys necessarily causes the fracture of superalloy components. To some extent, small inclusions can promote the refinement of the microstructure and improve the strength of high-temperature alloys during solidification. Only larger inclusions can induce the initiation of cracks and even fractures in the superalloy matrix. A critical oxide inclusion size exists, below which there is no reduction in fatigue life resulting from crack initiation at oxide inclusions, and above which there is a transition from slip-induced to inclusion-induced crack nucleation [14]. In summary, it is crucial to control the size of oxide inclusions in nickel-based superalloys.

Vacuum induction remelting is a method of secondary remelting to produce high-quality superalloy components [15]. As the final step before casting, the VIR process directly affects the characteristics of oxide inclusions in superalloy components. There are many ways to introduce oxide inclusions into Ni-based superalloys during the VIR process, for example, (i) in the quality of the master alloys for the remelting of Ni-based superalloys. There is no doubt that a low-purity master alloy is bound to introduce a large number of oxide inclusions into the Ni-based superalloy alloy melt [16]. (ii) In interface interactions between the crucible and superalloy melt, the interface interactions include the physical dissolution of the crucible inner wall by the melt and the chemical dissolution of the crucible particle in the melt [17]. Previous research has shown that high-melting-point inclusions are introduced when using an Al_2O_3 crucible to melt Ni-based superalloys [18,19]. (iii) Within the remelting parameters of Ni-based superalloys, the evidence presented thus far supports the idea that the vacuum level [20], smelting time [21], casting temperature [22], etc., can significantly affect the composition of the superalloy melt. In turn, this indirectly affects the oxide inclusions in the superalloy's components.

In this work, systematic research was meticulously conducted to explore the origins of oxide inclusions in a typical high-aluminum nickel-based superalloy during the VIR process. By employing thermal simulation smelting experiments combined with comprehensive thermodynamic calculations, this study investigated the formation mechanisms of oxide inclusions within a high-aluminum Ni-based superalloy. The insights gained from these calculations are aimed at elucidating the complex interactions and conditions that lead to the presence of oxide inclusions. It is anticipated that the findings from this research will significantly contribute to the broader scientific understanding of the potential formation mechanisms and offer strategic approaches for controlling oxide inclusions in Ni-based superalloys.

2. Materials and Methods

2.1. Experimental Materials

The experimental material in this study is a master high-aluminum Ni-based superalloy produced by the VIM process. In the VIR process, a 20 kg master alloy undergoes melting within a vacuum induction furnace set at 1873 K, with a vacuum level maintained at 0.5 Pa and a melting time of 20 min. Subsequently, the molten alloy is gradually cooled to 1823 K and held at this temperature for 3 min to ensure homogeneity and alleviate any remaining impurities. Following this refining stage, the refined metal is then carefully poured into a prepared mold, where it solidifies into its final form. Table 1 lists the nominal composition of the Ni-based superalloy before and after the VIR process. It is worth mentioning that the content of the active element Al in the Ni-based superalloy is 2–5%.

Table 1. The nominal composition of the high-aluminum Ni-based superalloy (wt. %).

Sample	Cr	Co	W	Al	Ta	Ti	Mo	C	B	Mg	Zr	Ni
VIM	11–14	7–11	3–6	2–5	3–7	3–6	1–3	0.03–0.1	trace	trace	trace	bal.
VIR	11–13	8–10	4–5	2–5	3–6	3–5	1–3	0.06–0.1	trace	trace	trace	bal.

In the vacuum induction refining process, a variety of crucibles, including alumina crucibles, magnesium oxide crucibles, and zirconia crucibles, are commonly utilized for melting. Each type of crucible offers distinct properties and benefits, making them suitable for specific applications and alloy compositions. For the vacuum melting process discussed in this study, a magnesium oxide crucible was selected due to its particular advantages, which will be thoroughly characterized and detailed in Section 3.1.

2.2. Oxide Inclusion Characterization Methods

Experimental samples for oxide inclusion characterization, cut from the core of the ignots, were prepared by electrodischarge machining. A field emission scanning electron microscope (FESEM, Crossbeam 550, Carl Zeiss AG, Oberkochen, Germany) equipped with an energy dispersive spectrometer (EDS, Ultim Max 65, Oxford, UK) was used to determine the oxide inclusion characteristics. The AZtecFeature automated particle analysis system, which incorporates a self-designed superalloy inclusion classification module, was used to quantitatively analyze the density, size distribution, and other characteristics of the oxide inclusions. The statistical area of the oxide inclusions in each sample was 2 mm $\times$ 1.5 mm, and oxide inclusions less than 300 nm in diameter were ignored in the statistical analysis.

It is worth noting that when statistically analyzing inclusions, we typically use a method that sequentially scans and collects data from multiple successive consecutive fields of view. In this experiment, we utilized a large field-of-view statistical technique specifically for analyzing oxide inclusions. This technique encompasses a substantial statistical area of 2 mm $\times$ 1.5 mm. The core principle of this method involves capturing 1000$\times$ magnification FESEM photographs, which are then concatenated to form a comprehensive and detailed overview. To enhance the accuracy and reliability of our statistical analysis, we took a total of 384 individual SEM photographs, covering the entire designated area. This extensive photographic dataset allows for a thorough and precise evaluation of the inclusions, ensuring that the data collected are both sufficient and representative.

In this work, the size of each oxide inclusion is represented by the equivalent circle diameter (ECD) with an equivalent plate area. According to the ECD results, the area fraction of the oxide inclusions in the experimental samples before and after the VIR process can be calculated. In order to further characterize the dispersion degree of the oxide inclusions in the samples, the test area was systematically divided into 300 smaller sections, each measuring 0.1 mm $\times$ 0.1 mm. This division allows for a detailed analysis of the distribution of oxide inclusions across the sample. The dispersion degree of the oxide inclusions is then quantified by calculating the standard deviation of the areal density of the oxide inclusions within each of these smaller areas. This statistical approach provides a comprehensive understanding of how uniformly the inclusions are distributed in the material before and after undergoing the VIR process.

3. Results

3.1. The Characteristics of the MgO Crucible Used in the VIR Process

Figure 1 shows the morphology and phase analysis of the MgO crucible. As shown in Figure 1a, the MgO crucible is composed of two main phases. The phase analysis of a single field of view was not statistically significant. Therefore, the phase analysis of the MgO crucible is carried out using large-area mapping combined with AutoPhaseMap analysis. The phase analysis results are shown in Figure 1b,c, indicating that the MgO crucible is composed of 87.35% of the MgO phase and 12.65% of the $MgO{\cdot}Al_2O_3$ phase, in terms of volume fraction. The analysis results are consistent with other research findings, and the

composition of the magnesium oxide melting crucible in the vacuum induction melting process consists of MgO and $MgO{\cdot}Al_2O_3$ phases.

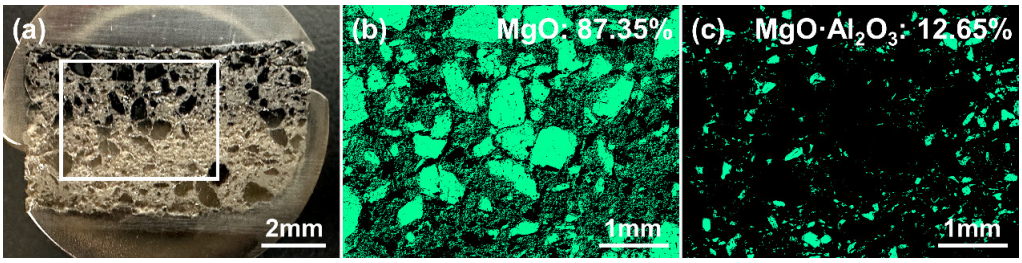

Figure 1. Phase analysis of the MgO crucible: (**a**) MgO crucible; a diagram of large-area mappings of (**b**) MgO and (**c**) $MgO{\cdot}Al_2O_3$ phase distributions.

In addition, the porous structure of the magnesium oxide crucibles can be clearly seen in Figure 1. Magnesium oxide crucibles are frequently prepared with a porous structure, primarily due to the high temperatures encountered during the vacuum melting process. This design choice is essential because dense structures tend to fracture under such conditions, often due to thermal expansion and other related stresses. The porous nature of these crucibles not only enhances their durability but also offers the additional benefit of being able to adsorb high melting point non-metallic or metallic oxides. This adsorption capability is crucial because it helps in trapping and retaining undesirable oxide inclusions, thereby improving the overall purity and quality of the molten metal.

3.2. Characteristics of Typical Oxide Inclusions before and after the VIR Process

3.2.1. The Morphology of Typical Oxide Inclusions

Figure 2 displays the morphology and EDS maps of the typical oxide inclusions found in the high-aluminum Ni-based superalloy before and after the VIR process. Figure 2a clearly shows that Mg, Al, and O are uniformly distributed throughout the inclusions, indicating that the typical oxide inclusions before the VIR process are made up of $MgO{\cdot}Al_2O_3$. In addition, many observational results show that most $MgO{\cdot}Al_2O_3$ inclusions are irregular in shape. Figure 2(b_1–b_4) displays the morphologies and EDS mappings of typical oxide inclusions found in the Ni-based superalloy after the VIR process. In the remelted superalloy, endogenous $MgO{\cdot}Al_2O_3$, film-like $MgO{\cdot}Al_2O_3$, exogenous $MgO{\cdot}Al_2O_3$, and exogenous MgO inclusions are detected, as shown in Figure 2(b_1–b_4), respectively. Figure 2(b_1) clearly shows that Mg, Al, and O are uniformly distributed throughout the inclusions, indicating that the typical oxide inclusions are composed of endogenous $MgO{\cdot}Al_2O_3$. Figure 2(b_2) shows that the film-like inclusions are composed of uniform Mg, Al, and O, indicating that the film-like inclusions are also $MgO{\cdot}Al_2O_3$. This may be because diluted air still exists in the vacuum during the VIR process, and the melt surface is rapidly oxidized. Therefore, when folded in or experiencing collisions between droplets, the surface oxide contacts the crucible liner when impinging against other masses of liquid [23]. This process may eventually lead to the formation of film-like $MgO{\cdot}Al_2O_3$. As shown in Figure 2(b_3), the exogenous $MgO{\cdot}Al_2O_3$ inclusions are on the millimeter scale. This may be the result of the large MgO crucible matrix spalling into the superalloy melt and reacting with the Al_2O_3 inclusions or the dissolved [Al] in the superalloy melt. The exogenous presence of several tens of microns of MgO inclusions, as shown in Figure 2(b_4), may also be caused by the spalling of the MgO crucible matrix.

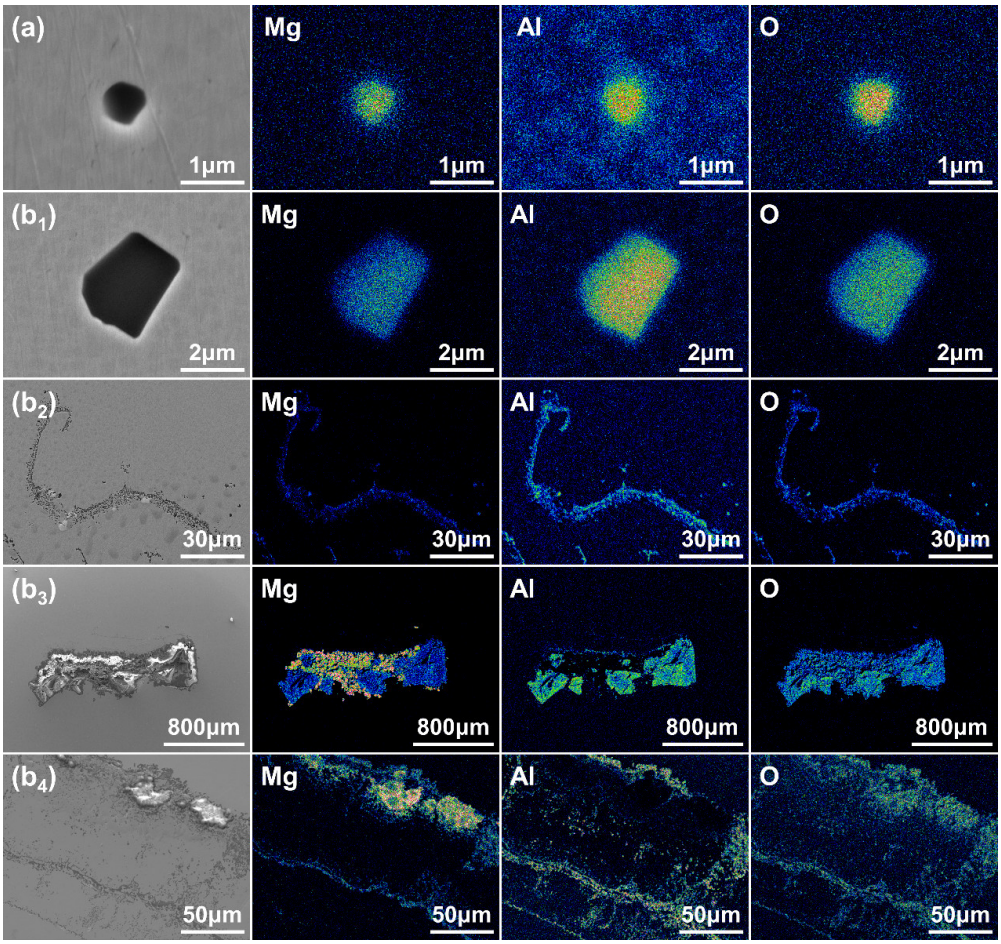

Figure 2. Morphologies and EDS mappings of typical oxide inclusions: (**a**) $MgO{\cdot}Al_2O_3$ inclusions found before the VIR process; (**b$_1$**) endogenous $MgO{\cdot}Al_2O_3$, (**b$_2$**) film-like $MgO{\cdot}Al_2O_3$, (**b$_3$**) exogenous $MgO{\cdot}Al_2O_3$, and (**b$_4$**) exogenous MgO inclusions found after the VIR process.

3.2.2. Types and Number Densities of Typical Oxide Inclusions

Table 2 summarizes the types and number densities of inclusions in the Ni-based superalloy before and after the VIR process. Based on the statistical results of the number of characteristics of oxide inclusions in high-aluminum Ni-based superalloys, the number densities of $MgO{\cdot}Al_2O_3$ before and after the VIR process are 62.67 and 45.00 mm^{-2}, respectively. It can be clearly seen that the VIR process can reduce the number density of $MgO{\cdot}Al_2O_3$ inclusions in the Ni-based superalloy. The decrease in the density of oxide inclusions is attributed to the porous material of the magnesium oxide crucible. As mentioned earlier, the magnesium oxide crucible used for vacuum melting is a porous material. During the VIR process, a portion of the oxide inclusions inside the alloy melt will be adsorbed inside the crucible, resulting in a decrease in the overall content of the oxides.

Table 2. The types and number densities of endogenous inclusions in high-aluminum Ni-based superalloys before and after the VIR process.

Process	Type	Number	Area, mm	Number Density, mm^{-2}
VIM	$MgO{\cdot}Al_2O_3$	188	3	62.67
VIR	$MgO{\cdot}Al_2O_3$	145	3	45.00

3.2.3. The Size Distribution and Dispersion Degree of Typical Oxide Inclusions

The strength, toughness, and fatigue resistance of Ni-based superalloys are closely related to the size distribution and dispersion degree of oxide inclusions [24–26]. Therefore,

describing these characteristics of oxide inclusions in Ni-based superalloys is crucial. The size of each oxide inclusion is represented by the equivalent circle diameter with an equivalent plate area. The dispersion degree is described by the standard deviation of the areal density of oxide inclusions for each small area.

Figure 3 shows the statistical results of the size distribution and dispersion degree of the oxide inclusions in the high-aluminum Ni-based superalloy before and after the VIR process. As shown in Figure 3a, the average $MgO{\cdot}Al_2O_3$ inclusion size before the VIR process is 0.64 μm. Most of the oxide inclusions, accounting for 99.49% of the total number of inclusions, are smaller than 2 μm. According to the ECD results, the area fraction of the inclusions in the sample before the VIR process is 0.00264%. Figure 3b reveals the average areal density of the oxide inclusions before the VIR process, and the standard deviation is 1.180, indicating that the sizes of the $MgO{\cdot}Al_2O_3$ inclusions before the VIR process are not relatively uniform. As shown in Figure 3c, the average oxide inclusion size after the VIR process is 0.76 μm. Most of the oxide inclusions, accounting for 95.10% of the total number of inclusions, are smaller than 2 μm. Compared with the average size of oxide inclusions before the VIR process, the size of the inclusions increases, which is the inevitable result of the aggregation and growth of oxide inclusions during the VIR process. According to the ECD results, the area fraction of inclusions in the sample after the VIR process is 0.00335%. Figure 3d reveals the average areal density of the oxide inclusions after the VIR process, and the standard deviation is 0.737, indicating that the sizes of the $MgO{\cdot}Al_2O_3$ inclusions after the VIR process are more uniform than those before the VIR process. Therefore, the statistical results show that the VIR process can increase the oxide inclusion size and dispersion degree of inclusions to a certain extent in high-aluminum Ni-based superalloys.

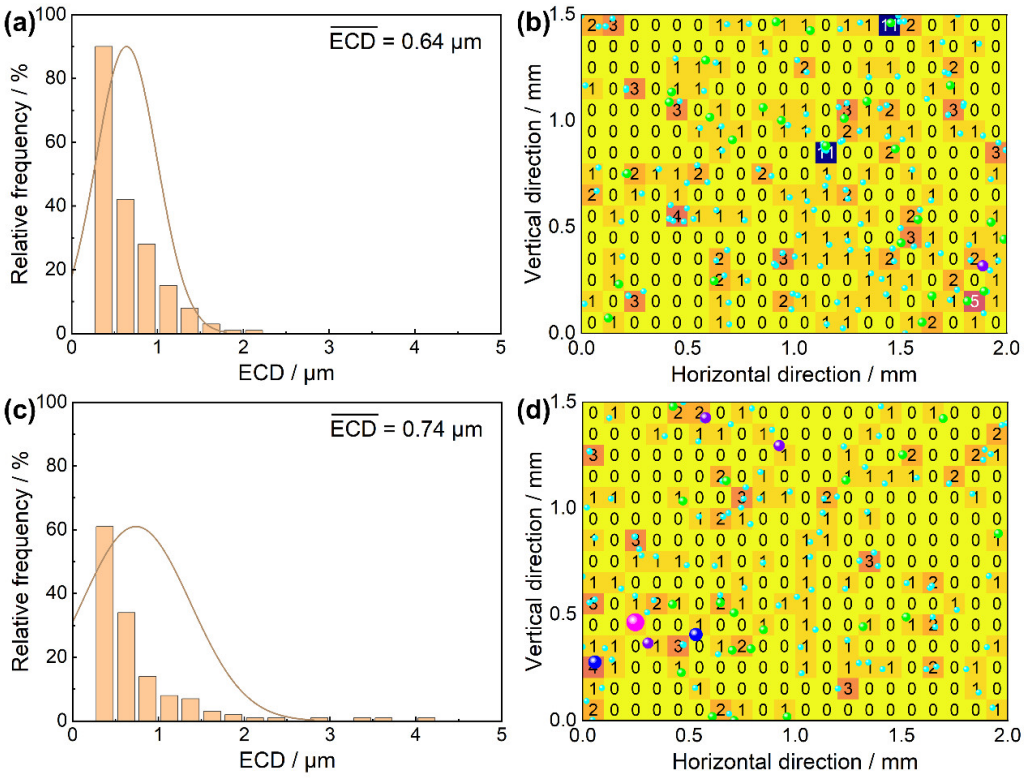

Figure 3. The statistical results of endogenous $MgO{\cdot}Al_2O_3$ inclusions: (**a**) the size distribution (**b**) and areal density distribution before the VIR process, (**c**) and the size distribution and (**d**) areal density distribution after the VIR process. (cyan ball: <1 μm, green ball: 1–2 μm, purple ball: 2–3 μm, blue ball: 3–4 μm, pink ball: 4–5 μm).

4. Discussion

4.1. The Formation Mechanism of Endogenous Irregular MgO·Al_2O_3 Inclusions after the VIR Process

The compositions of the typical small inclusions in the experimental samples before and after the VIR process at room temperature are consistent with each other, indicating that the endogenous MgO·Al_2O_3 inclusions after the VIR process are mainly derived from the master alloy. To verify our hypothesis, the phase transformation and oxide precipitation behavior before and after the addition of Mg to the molten alloy during the VIM process were calculated using FactSage 8.3 software.

The thermodynamic equilibrium calculations before and after the addition of Mg to the molten alloy are shown in Figure 4a,b, respectively. As shown in Figure 4a, the oxide inclusions before Mg's addition only existed in the form of the CORU#1 phase above 1573 K. The CORU#1 phase consisted of Al_2O_3 containing trace amounts of Ti_2O_3, Cr_2O_3, Fe_2O_3, and Mn_2O_3. However, after the addition of Mg, as shown in Figure 4b, oxide inclusions only existed in the form of the TiSp phase above 1583 K. The TiSp phase is $MgAl_2O_4$ and contains trace amounts of $MgTi_2O_4$, $MnTi_2O_4$, and $FeTi_2O_4$. The above experimental results show that the typical oxide inclusion before the VIR process is MgO·Al_2O_3, which is consistent with the calculation results. Notably, the typical oxide inclusion after the VIR process is also MgO·Al_2O_3, indicating that the VIR process has no significant influence on the composition of inclusions in high-aluminum Ni-based superalloys.

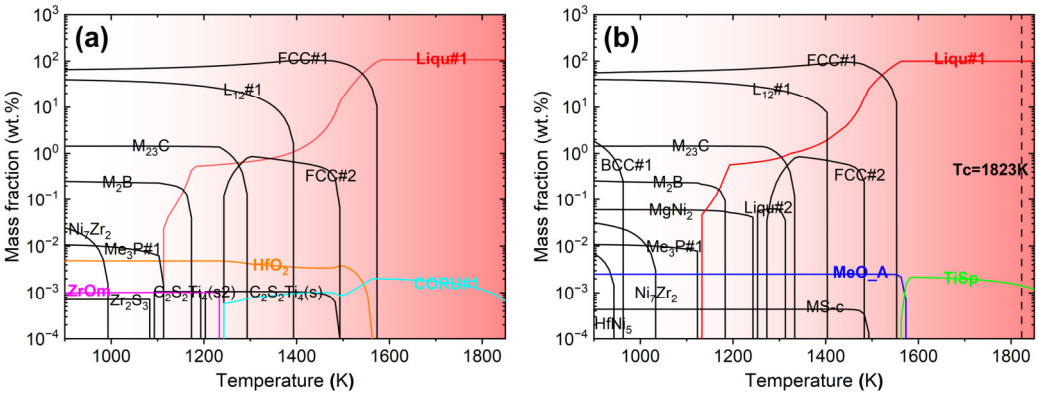

Figure 4. The thermodynamic equilibrium calculation results (**a**) before Mg's addition and (**b**) after Mg's addition during solidification.

4.2. The Formation Mechanism of Film-like MgO·Al_2O_3 Inclusions after the VIR Process

As shown in Figure 5, SEM and EDS mapping were performed to investigate the interface morphologies and distributions of the main elements between the MgO crucible and the high-aluminum Ni-based superalloy after the VIR process. As shown in Figure 5a, b, several hundred microns of massive and elongated inclusions are easily observed. In addition, there is a dark reaction layer on the MgO crucible side and the superalloy side. To determine the composition of the two dark reaction layers, EDS mapping analysis was performed on the regions. Figure 5c clearly shows that the interface is mainly composed of a MgO·Al_2O_3 layer and an Al_2O_3 layer near the MgO crucible side. The MgO·Al_2O_3 layer is much thinner than the Al_2O_3 layer and has a thickness of approximately 3.60 μm compared to 19.94 μm. The morphology and EDS mappings near the superalloy side are shown in Figure 5d. The interface is mainly composed of an Al_2O_3 inclusion layer near the superalloy side at approximately 1.51 μm. Large, film-like MgO·Al_2O_3 and Al_2O_3 inclusions are also detected at the interface between the MgO crucible and the superalloy. This may be due to the adsorption of Al_2O_3 inclusions in the melt by the inner wall of the MgO crucible and the subsequent solid–solid reaction to form film-like MgO·Al_2O_3, which is ultimately involved in the superalloy melt.

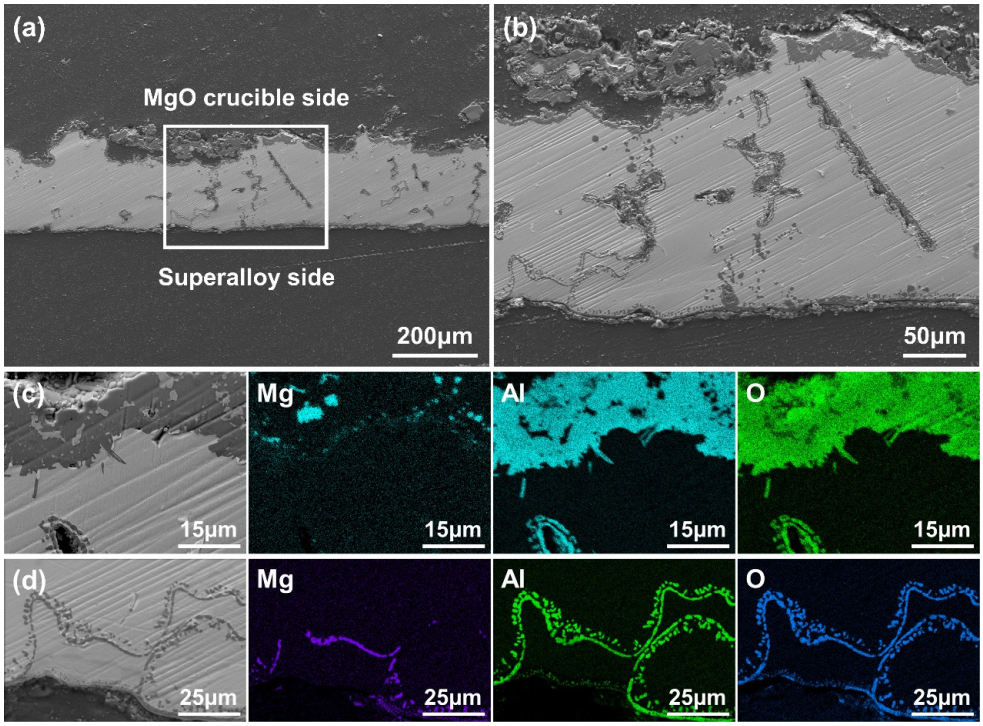

Figure 5. The morphologies and EDS maps of the interface between the MgO crucible and the high-aluminum Ni-based superalloy after the VIR process. (**a**) Low-magnification SEM image; (**b**) high-magnification SEM image; (**c**) morphologies and EDS mappings near the MgO crucible side; (**d**) morphologies and EDS mappings near the superalloy side.

To verify the above hypothesis, thermodynamic calculations were performed to explore the effect of the crucible and alloy melt interface reaction during the VIR process on the formation of oxide inclusions in the final superalloy components. The thermodynamic calculations of the interfacial reaction between the MgO crucible and the high-aluminum Ni-based superalloy at 1823 K are shown in Figure 6. The MeO_A phase consists of MgO containing trace amounts of Al_2O_3, Cr_2O_3, ZrO_2, etc., while the TiSp phase consists of $MgAl_2O_4$ containing trace amounts of $MgTi_2O_4$, $MnTi_2O_4$, $FeTi_2O_4$, etc. It can be clearly seen that a large amount of the TiSp phase appears at the interface near the alloy melt side. As the distance from the melt side increases, the content of the TiSp phase increases. The calculated results are consistent with the experimental results, demonstrating that the interfacial reaction between the crucible and superalloy melt during the VIR process introduces many $MgO{\cdot}Al_2O_3$ inclusions into the interface.

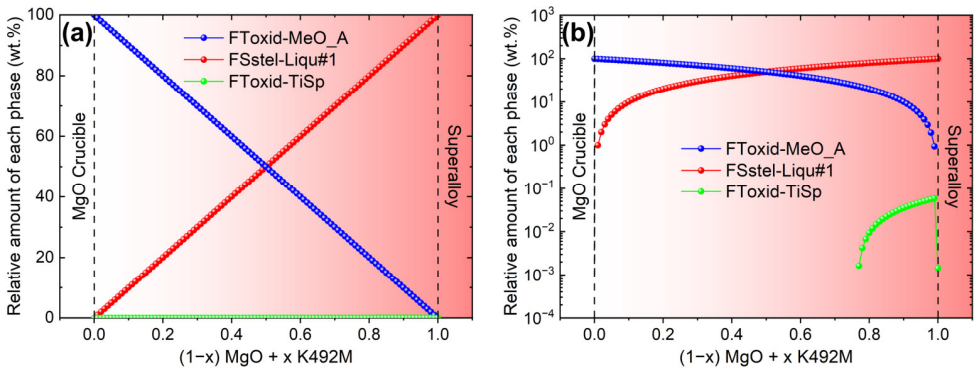

Figure 6. The thermodynamic calculation results of the interfacial reaction between the MgO crucible and the high-aluminum Ni-based superalloy at 1823 K: (**a**) the linear coordinate system and (**b**) the logarithmic coordinate system.

During the VIR process, Al_2O_3 inclusions may exist in the superalloy melt due to the so-called vacuum, which must be viewed as merely diluted air. The dissolved [Al] in a high-aluminum Ni-based superalloy melt can easily react with oxygen in diluted air to form Al_2O_3 inclusions. To further determine the mechanism responsible for the formation of $MgO{\cdot}Al_2O_3$ inclusions between the MgO crucible and the high-aluminum Ni-based superalloy after the VIR process, the Al-MgO and Al_2O_3-MgO phase diagrams were calculated, as shown in Figure 7a,b, respectively. Clearly, Al cannot directly react with MgO, while Al_2O_3 can react with MgO to form $MgAl_2O_4$. At the casting temperature, the reaction between MgO and Al_2O_3 is efficient, requiring only 0.10% Al_2O_3. Therefore, the $MgO{\cdot}Al_2O_3$ inclusions at the interface are the result of an in situ solid–solid reaction between the MgO crucible and the Al_2O_3 inclusions in the superalloy melt.

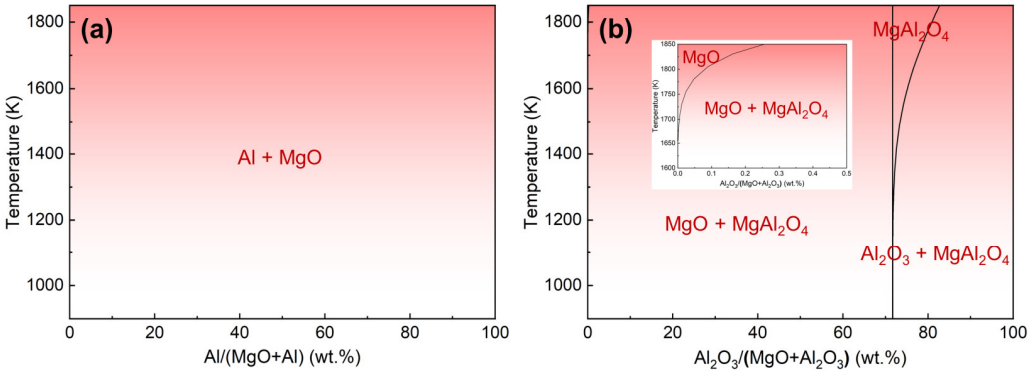

Figure 7. Binary phase diagrams: (**a**) Al-MgO and (**b**) Al_2O_3-MgO.

4.3. The Formation Mechanism of Large $MgO{\cdot}Al_2O_3$ and MgO Inclusions after the VIR Process

Overall, the formation mechanism of $MgO{\cdot}Al_2O_3$ inclusions at the interface can be summarized as follows: (i) the dissolved [Al] in the superalloy melt reacts with O_2 to form Al_2O_3 inclusions; (ii) Al_2O_3 inclusions randomly adhere to the inner wall of the MgO crucible; (iii) an in situ solid–solid phase reaction occurs between the Al_2O_3 and MgO at the interface to form $MgO{\cdot}Al_2O_3$ inclusions; and (iv) the $MgO{\cdot}Al_2O_3$ inclusions that form at the interface peel off and entrap into the superalloy melt. The detailed formation process of $MgO{\cdot}Al_2O_3$ inclusions in the high-aluminum Ni-based superalloy during the VIR process is illustrated in Figure 8, which provides a visual representation of each step in the mechanism. This understanding is crucial for developing strategies to control and minimize the presence of such inclusions in high-aluminum nickel-based superalloys.

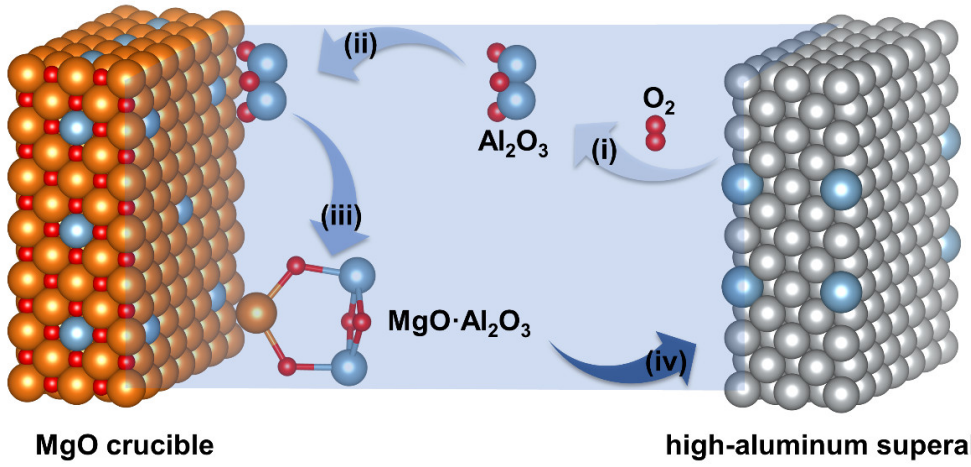

Figure 8. The formation mechanism of large $MgO{\cdot}Al_2O_3$ inclusions in the high-aluminum Ni-based superalloy during the VIR process.

5. Conclusions

The evolution and formation mechanism of oxide inclusions in a high-aluminum Ni-based superalloy were quantitatively investigated through a combination of experiments and thermodynamic calculations during the VIR process. The main conclusions are summarized as follows:

(1) The typical oxide inclusions in the master alloy and high-aluminum Ni-based superalloy after the VIR process are both made up of irregular $MgO{\cdot}Al_2O_3$. The VIR process effectively reduced the number density of the oxide inclusions in the high-aluminum Ni-based superalloy from 62.67 to 45.00 mm^{-2}. Simultaneously, the average oxide inclusion size increases from 0.64 to 0.74 μm, the area fraction of inclusions increases from 0.00264 to 0.00335%, and the standard deviation of the areal density of the oxide inclusions decreases from 1.180 to 0.737, indicating an increase in oxide inclusion uniformity.

(2) While the VIR process demonstrates efficacy in reducing oxide inclusions, it introduces millimeter-scale oxide inclusions, several tens of microns of MgO inclusions, and large micron-scale film inclusions into high-aluminum Ni-based superalloys. It is imperative to rigorously eliminate these introduced inclusions. Consequently, selecting a high-quality crucible during the smelting process is of paramount importance.

(3) The VIR process in high-aluminum Ni-based superalloys involves three primary formation mechanisms for $MgO{\cdot}Al_2O_3$. These mechanisms include the heredity of oxide inclusions, the interfacial reaction between the MgO crucible and the high-aluminum superalloy melt, and the exfoliation and entrapment of the inner wall of the MgO crucible, which adsorbs Al_2O_3 inclusions and undergoes chemical reactions. The second three mechanisms introduce several hundred micron-thick film-like and bulk millimeter-scale $MgO{\cdot}Al_2O_3$ inclusions.

Author Contributions: Conceptualization, Y.Z. and M.X.; methodology, M.X.; software, E.L. and W.F.; validation, W.X., Z.X. and W.F.; formal analysis, L.Z., W.X. and C.G.; investigation, Y.L.; resources, C.G.; data curation, Y.L.; writing—original draft preparation, E.L.; writing—review and editing, E.L. and W.X.; visualization, Z.X.; supervision, M.X.; project administration, L.Z. and Y.Z.; funding acquisition, L.Z. and Y.Z. All authors have read and agreed to the published version of the manuscript.

Funding: This research was supported by the National Natural Science Foundation of China (No. 52374360).

Data Availability Statement: The raw data supporting the conclusions of this article will be made available by the authors on request.

Conflicts of Interest: Author Lihui Zhang, Weijie Xing, Yunsong Zhao, Yushi Luo was employed by the company Beijing Institute of Aeronautical Materials. The remaining authors declare that the research was conducted in the absence of any commercial or financial relationships that could be construed as a potential conflict of interest.

References

1. Yang, C.; Hu, R.; Wang, X.; Du, J.; Luo, X.; Bi, Z.; Gan, B. Effect of pre-tensile treatments on the mechanical properties and deformation mechanism of a novel Ni-based superalloy. *Mater. Sci. Eng. A* **2023**, *874*, 145063. [CrossRef]
2. Juillet, C.; Oudriss, A.; Balmain, J.; Feaugas, X.; Pedraza, F. Characterization and oxidation resistance of additive manufactured and forged IN718 Ni-based superalloys. *Corros. Sci.* **2018**, *142*, 266–276. [CrossRef]
3. Detrois, M.; Antonov, S.; Rozman, K.A.; Hawk, J.A.; Jablonski, P.D. Improved creep and tensile properties of a corrosion resistant Ni-Based superalloy using high temperature aging and Nb/Ta additions. *Metall. Mater. Trans. A* **2022**, *53*, 2600–2613. [CrossRef]
4. Wang, J.; Wang, L.; Li, J.; Chen, C.; Yang, S.; Li, X. Effects of aluminum and titanium additions on the formation of nonmetallic inclusions in nickel-based superalloys. *J. Alloys Compd.* **2022**, *906*, 164281. [CrossRef]
5. Bergsmo, A.; Xu, Y.; Poole, B.; Dunne, F.P.E. Twin boundary fatigue crack nucleation in a polycrystalline Nickel superalloy containing non-metallic inclusions. *J. Mech. Phys. Solids* **2022**, *160*, 104785. [CrossRef]
6. Yao, Z.; Hou, J.; Chen, Y.; Xu, W.; Jiang, H.; Dong, J. Effect of micron-sized particles on the crack growth behavior of a Ni-based powder metallurgy superalloy. *Mater. Sci. Eng. A* **2022**, *860*, 144242. [CrossRef]

7. Liu, P.; Jiang, H.; Dong, J.; Chen, Z. Effect of micron-scale nonmetallic inclusions on fatigue crack nucleation in a nickel-based superalloy. *Int. J. Solids Struct.* **2023**, *279*, 112368. [CrossRef]
8. Texier, D.; Stinville, J.C.; Echlin, M.L.P.; Pierret, S.; Villechaise, P.; Pollock, T.M.; Cormier, J. Short crack propagation from cracked non-metallic inclusions in a Ni-based polycrystalline superalloy. *Acta Mater.* **2019**, *165*, 241–258. [CrossRef]
9. Zhao, Y.; Wang, L.; Chen, C.; Li, J.; Li, X. Effect of a MgO–CaO–ZrO_2-based refractory on the cleanliness of a K4169 Ni-based superalloy. *Ceram. Int.* **2023**, *49*, 117–125. [CrossRef]
10. Gao, R.; Li, L.; Chen, C.; Li, J.; Wang, L.; Li, X.; Yang, H. Formation and aggregation behavior of inclusions in Ni-based alloys with different Mg contents. *J. Mater. Res. Technol.* **2023**, *26*, 5252–5263. [CrossRef]
11. Miller, C.F.; Simmons, G.W.; Wei, R.P. Mechanism for oxygen enhanced crack growth in inconel 718. *Scr. Mater.* **2001**, *44*, 2405–2410. [CrossRef]
12. Jiang, R.; Ji, D.; Shi, H.; Hu, X.; Song, Y.; Gan, B. Effects of thermal exposure on high-cycle-fatigue behaviours in Ni-based superalloy GH4169. *Mater. Sci. Technol.* **2019**, *35*, 1265–1274. [CrossRef]
13. Yang, S.; Yang, S.; Qu, J.; Du, J.; Gu, Y.; Zhao, P.; Wang, N. Inclusions in wrought superalloys: A review. *J. Iron Steel Res. Int.* **2021**, *28*, 921–937. [CrossRef]
14. Chan, K.S. A fatigue life model for predicting crack nucleation at inclusions in Ni-based superalloys. *Metall. Mater. Trans. A* **2020**, *51*, 1148–1162. [CrossRef]
15. Akande, I.G.; Oluwole, O.O.; Fayomi, O.S.I.; Odunlami, O.A. Overview of mechanical, microstructural, oxidation properties and high-temperature applications of superalloys. *Mater. Today Proc.* **2021**, *43*, 2222–2231. [CrossRef]
16. Gao, X.; Zhang, L.; Qu, X.; Luan, Y.; Chen, X. Investigation on the formation mechanism of non-metallic inclusions in high-aluminum and titanium-alloyed Ni-based superalloy. *Vacuum* **2020**, *177*, 109409. [CrossRef]
17. Liu, Y.; Gao, Y.; Wang, E.; Chen, G.; Xu, E.; Zhao, F.; Zhao, Y.; Li, C.; Hou, X. Interaction between CA_6-MA crucible and molten wrought Ni-based superalloys. *J. Eur. Ceram. Soc.* **2023**, *43*, 1714–1722. [CrossRef]
18. Song, Q.; Qian, K.; Shu, L.; Chen, B.; Ma, Y.; Liu, K. Interfacial reaction between nickel-based superalloy K417G and oxide refractories. *Acta Metall. Sin.* **2021**, *58*, 868–882.
19. Gao, X.; Zhang, L.; Qu, X.; Chen, X.; Luan, Y. Effect of interaction of refractories with Ni-based superalloy on inclusions during vacuum induction melting. *Int. J. Miner. Metall. Mater.* **2020**, *27*, 1551–1559. [CrossRef]
20. Li, J.; Zhang, H.; Gao, M.; Li, Q.; Liu, H.; Zhang, H. Effect of vacuum level on the interfacial reactions between K417 superalloy and Y_2O_3 crucibles. *Vacuum* **2020**, *182*, 109701. [CrossRef]
21. Yiliti, Y.; Dong, G.; Liu, X.; You, X.; Han, W.; Dong, L.; Zhao, Y.; Yi, L.; Wang, Y. The high temperature oxidation behavior of a superalloy prepared by vacuum induction melting and electron beam smelting: A comparative study. *J. Mater. Res. Technol.* **2023**, *25*, 6977–6991. [CrossRef]
22. You, X.; Dong, G.; Zhou, H.; Zhang, H.; Tan, Y.; Wang, Y.; Li, P.; You, Q.; Li, Y.; Cui, H.; et al. Removal of oxygen, nitrogen, and inclusions in powder superalloy scraps by electron beam smelting and induced solidification and the purification mechanisms. *Sep. Purif. Technol.* **2023**, *304*, 122290. [CrossRef]
23. Campbell, J.; Tiryakioğlu, M. Bifilm defects in Ni-based alloy castings. *Metall. Mater. Trans. B* **2012**, *43*, 902–914. [CrossRef]
24. Jiang, J.; Yang, J.; Zhang, T.; Dunne, F.P.E.; Britton, T.B. On the mechanistic basis of fatigue crack nucleation in Ni superalloy containing inclusions using high resolution electron backscatter diffraction. *Acta Mater.* **2015**, *97*, 367–379. [CrossRef]
25. Hu, D.; Wang, T.; Ma, Q.; Liu, X.; Shang, L.; Li, D.; Pan, J.; Wang, R. Effect of inclusions on low cycle fatigue lifetime in a powder metallurgy nickel-based superalloy FGH96. *Int. J. Fatigue* **2019**, *118*, 237–248. [CrossRef]
26. Zheng, L.; Zhang, G.; Gorley, M.J.; Lee, T.L.; Li, Z.; Xiao, C.; Tang, C.C. Effects of vacuum on gas content, oxide inclusions and mechanical properties of Ni-based superalloy using electron beam button and synchrotron diffraction. *Mater. Des.* **2021**, *207*, 109861. [CrossRef]